http://www.aimspress.com/journal/mine

Mathematics in Engineering, 1(3): 489–507.
DOI:10.3934/mine.2019.3.489
Received: 11 December 2018
Accepted: 19 April 2019
Published: 03 June 2019

Research article

Breathers and other time-periodic solutions in an array of cantilevers decorated with magnets†

Christopher Chong[1,*], Andre Foehr[2,3], Efstathios G. Charalampidis[4], Panayotis G. Kevrekidis[4] and Chiara Daraio[3]

[1] Department of Mathematics, Bowdoin College, Brunswick, Maine 04011, USA
[2] Department of Mechanical and Process Engineering (D-MAVT), Swiss Federal Institute of Technology (ETH), 8092 Zürich, Switzerland
[3] Division of Engineering and Applied Science, California Institute of Technology, Pasadena, CA, USA
[4] Department of Mathematics and Statistics, University of Massachusetts, Amherst, MA 01003-4515, USA

† **This contribution is part of the Special Issue:** Hamiltonian Lattice Dynamics
Guest Editors: Simone Paleari; Tiziano Penati
Link: http://www.aimspress.com/newsinfo/1165.html

* **Correspondence:** Email: cchong@bowdoin.edu; Tel: +12077253577; Fax: +12077253750.

Abstract: In this article, the existence, stability and bifurcation structure of time-periodic solutions (including ones that also have the property of spatial localization, i.e., breathers) are studied in an array of cantilevers that have magnetic tips. The repelling magnetic tips are responsible for the intersite nonlinearity of the system, whereas the cantilevers are responsible for the onsite (potentially nonlinear) force. The relevant model is of the mixed Fermi-Pasta-Ulam-Tsingou and Klein-Gordon type with both damping and driving. In the case of base excitation, we provide experimental results to validate the model. In particular, we identify regions of bistability in the model and in the experiment, which agree with minimal tuning of the system parameters. We carry out additional numerical explorations in order to contrast the base excitation problem with the boundary excitation problem and the problem with a single mass defect. We find that the base excitation problem is more stable than the boundary excitation problem and that breathers are possible in the defect system. The effect of an onsite nonlinearity is also considered, where it is shown that bistability is possible for both softening and hardening cubic nonlinearities.

Keywords: breather; time-periodic; Fermi-Pasta-Ulam-Tsingou; Klein-Gordon; cantilever array; magnet

1. Introduction

The subject of nonlinear lattices has been, and continues to be, an intensely studied area of research [1, 2], with prototypical examples being the Fermi-Pasta-Ulam-Tsingou (FPUT) and Klein-Gordon (KG) models. One particular structure of interest in nonlinear lattices is the so-called discrete breather, which is a solution that is localized in space and periodic in time. Discrete breathers (or just breathers) have been studied in a variety of physical systems, including, optical waveguide arrays and photorefractive crystals [3], Josephson-junction ladders [4, 5], layered antiferromagnetic crystals [6, 7], halide-bridged transition metal complexes [8], dynamical models of the DNA double strand [9], Bose-Einstein condensates in optical lattices [10], and many others. One mechanical realization of a nonlinear lattice that has attracted significant attention is the so-called granular chain. Granular chains consist of closely packed arrays of particles that interact elastically [11]. The contact force can be tuned to yield near linear to purely nonlinear responses, and the effective stiffness properties can also be easily changed by modifying the material, geometry, or contact angle of the elements in contact [11]. This remarkable tunability has made the topic of granular chains an active research area over the past two decades (see the books [11–13] and review articles [14–16]). Despite this tunability, there are some limitations to granular chains. For example, it is difficult to excite an arbitrary node in the chain*. Adding an onsite force to the granular chain (to realize e.g., the cradle problem [19]) is also challenging from an experimental perspective.

Motivated by these considerations, the present work considers a system of macroscopic cantilevered beams that are coupled via magnetic links. This system is highly tunable, like the granular chain, but also allows the possibility to excite arbitrary nodes in the array and offers additional tunability in the form of an onsite force that is introduced via the cantilever. While a linear onsite force is considered for the experimental aspect of this paper, nonlinear forces will be also explored numerically. The relevant model equation we derive (in the more general case where the beam can be nonlinear) is of the so-called mixed FPUT-KG type, meaning there are both intersite and onsite nonlinear forces. In terms of breather solutions, it is well known that the site-centered† solutions are spectrally stable in Hamiltonian lattices with onsite nonlinearities (e.g., KG lattices) and bond-centered‡ breathers are unstable. In the presence of an intersite nonlinearity (so that the model is of the mixed FPUT-KG type) the stability of site-centered and bond-centered solutions are exchanged at a critical value of the intersite nonlinearity coefficient [20].

The system considered herein is a macroscopic analog of the micromechanical cantilever arrays considered in, e.g., Ref. [21], where the cantilevers are coupled via the geometry of the base (as opposed to via magnetic links, as in our system) and the motion is perpendicular to the transverse direction of the base (as opposed to along transverse direction of the base, as in our system). There

*Typically, excitations are on the boundary. While internal resonators can be used to excite internal modes [17, 18], their presence introduces a defect into the system

†A site-centered breather is a solution that is centered at a lattice site

‡A bond-centered breather is a solution that is centered in between two lattice sites

too, the relevant model is a mixed FPUT-KG equation. The microcantilever experiments of [21], however, were conducted in a vacuum to eliminate damping from the model considerations, and thus Hamiltonian dynamics were studied. For our experimental set-up, the Hamiltonian variant is a possible approximate model, however the effects of damping are non-negligible due to the scale of the system. Therefore, the focus of this article will be on a damped-driven, mixed FPUT-KG equation. In particular, time-periodic excitations, including breathers, will be studied. In this respect, our paper can be thought of as a damped-driven extension of the paper [20].

The present paper is organized as follows: In Section 2 we describe the experimental set-up which is modeled in Section 3. We explore the linear problem and outline the numerical methods for the computation of periodic orbits in Section 4. After validating the model in Section 5 via direct comparison with experimental results, we present a number of numerical results in Section 6 concerning the existence, stability and bifurcation structure of time-periodic solutions in various set-ups, including homogeneous ones under various excitations and defect ones. Section 7 concludes the paper.

2. Experimental set-up

The array of cantilevers we consider is fixed to a rigid aluminum slab [Figure 1 (center)]. The boundaries of the array are also rigid aluminum slabs with magnets at their tops. Using 3D printed holders, we also embed three magnets within the tip of each cantilevers (right, 6 mm × 4 mm × 2 mm from supermagnete.ch) and orient them along the vertical axis such that the cantilevers repel each other. A phospher bronze metal sheet (M3) from Hassler-Profile is used to manufacture the cantilevers. The base of the cantilever array is guided to move freely along the direction of the first flexural resonance mode of the cantilever.

We use a shaker (Brüel & Kjær Type-4810) driven by an audio amplifier (Topping TP22) to excite the base of the cantilever array. A lock-in amplifier is used to generate the excitation signal and filter the measured velocity of the base (bottom, Zurich Instruments HF2LI). We acquire the velocity of the base using a laser Doppler vibrometer (Polytec OFV-505, Polytec OFV-5000). The positions of the cantilever tips are acquired at 400 fps using a high speed camera (Vision Research Phantom v1610). Subsequently, we use digital image correlation (DIC) to calculate sub-pixel-resolution positions of the cantilever tips (VIC 2D). Additionally, we use an oscilloscope (Tektronix DPO3014) to acquire the time-domain signals.

To characterize the system we start by considering a single cantilever with no magnets on the system boundaries. We measure the geometric parameters of the cantilever using a caliper and the tip mass using a scale (Table 1). By measuring the dynamic response of the single cantilevers we can experimentally characterize the resonance frequency and the damping characteristics of the cantilevers as shown in Figure 2. The damping coefficient γ is estimated from the damping ratio ξ, which is estimated using

$$\xi = \frac{1}{f_0}\frac{\partial f}{\partial \phi},$$

where $\frac{\partial \phi}{\partial f}$ is the slope of the phase with respect to the swept frequency at the resonance frequency f_0. Using the tabulated material properties of the phosphor bronze (Table 1) and the other geometric parameters, we predict a resonance frequency of 53.66 Hz (using the methods outlined in Section 3).

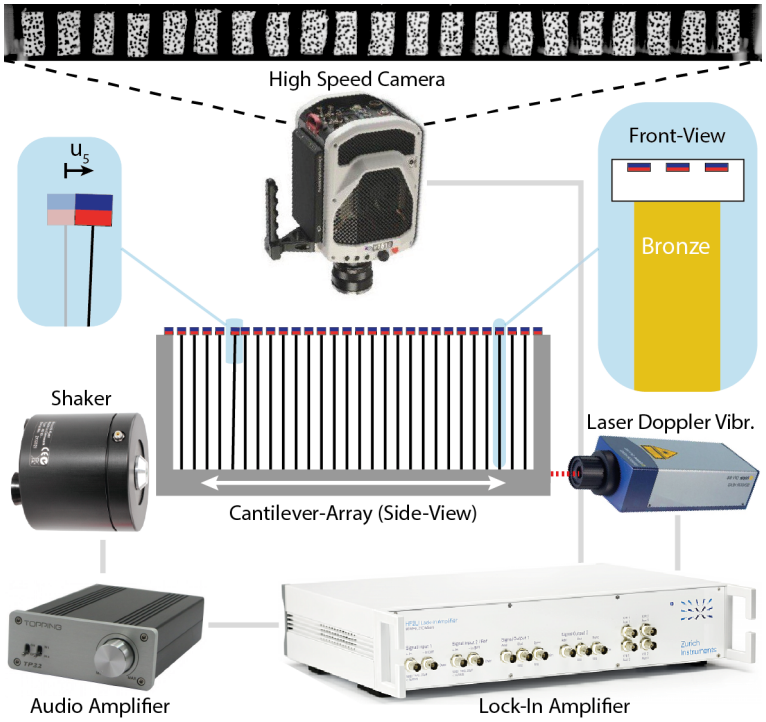

Figure 1. Schematic of the experimental set-up.

Experimentally, we found a median resonance frequency of 50.41 Hz. We believe the 6% frequency shift is due to the added flexibility from the fixation of the cantilever that uses small screw connections. To optimize the model, we subsequently estimate the stiffness of the analytical model using the measured resonance frequency and the effective mass.

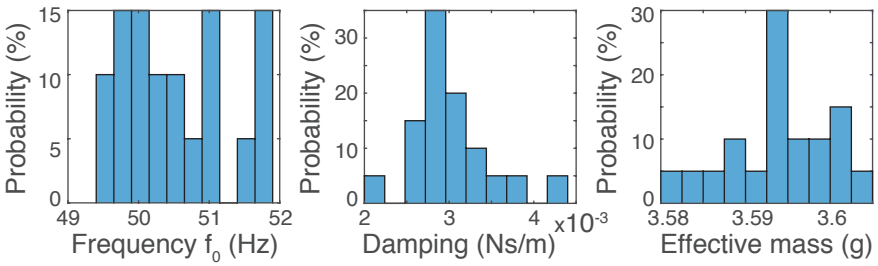

Figure 2. Probability distribution of the cantilever resonance frequency (left), the damping coefficient (center) and the effective mass of the cantilever model (right). We use the median values for Table 1.

Table 1. (Left) Geometric and physical parameters of the set-up and (right) the estimated parameters of the analytical model.

Description	Symbol	Value	Description	Symbol	Value
Length	L	59.15 mm	Effective mass	m	3.594 g
Width	w	23 mm	Onsite stiffness	κ	361.1 N/m
Thickness	h	0.5 mm	Onsite nonlinearity	β	0
Density	ρ	$8.8 \cdot 10^3$ kg/m^3	Damping coefficient	γ	$2.95 \cdot 10^{-3}$ Ns/m
Young's modulus	Y	118 GPa	Magnet distance	d_0	6.3993 mm
Damping coefficient	γ	$2.95 \cdot 10^{-3}$ Ns/m	Magnet coefficient	A	$2.942 \cdot 10^{-8}$ N/m^p
Top mass	M_t	2.162 g	Magnet exponent	p	-3.412

We then characterize the force deflection relationship of the magnets using an Instron E3000. Figure 3 shows the measured data and an approximation of the force deflection relationship using

$$F_{mag}(d) = Ad^p = A(d_0 + \Delta d)^p,$$

where A, p are the fitting parameters. The distance d can be separated into two parts, d_0 (the initial distance) and Δd (additional deflection). See Table 1. We estimate the inter-magnet distance d_0 by measuring the distance between the outermost magnets and averaging this distance after removing one magnet-width (Table 1).

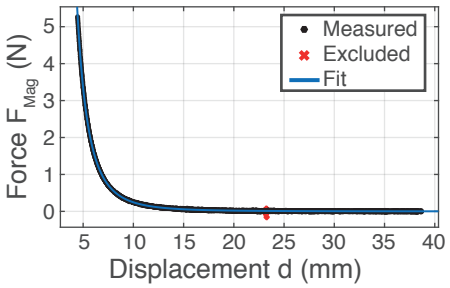

Figure 3. Characterization of the magnetic interaction forces: The black dots and the red crosses are experimental measurements. We exclude the noisy data (red crosses) for the estimation of the fitting function (blue curve). The experimental data is well described by the fitting function which follows the centerline of the measured force.

3. Model derivation

We first consider a single beam that is cantilevered to a movable base. If the displacement of the base is $y(t)$ and the displacement of the tip of the beam is $x(t)$ then the lumped-parameter model for the dynamics of the beam tip is given by [22],

$$m\ddot{x} + \gamma(\dot{x} - \dot{y}) + \kappa(x - y) = 0 \tag{3.1}$$

where the dot stands for differentiation with respect to time t and m, γ, κ are the so-called effective mass, damping coefficient, and stiffness, respectively. This model is derived by considering only the

fundamental mode of vibration from the Euler-Bernoulli model of a clamped beam. Through this derivation, one finds the effective stiffness to be

$$\kappa = \frac{3YI}{L^3}$$

where YI is the beam's bending stiffness and L is the length of the beam. If a tip mass is present (which is the case in our system), the effective mass is found by expressing the total kinetic energy of the beam in terms of the velocity at the tip through the Rayleigh quotient [22],

$$m = \frac{33}{140}\tilde{m}L + M_t$$

where $\tilde{m}$ is the mass per unit length of the beam and M_t is the mass of the tip. The effective damping coefficient is

$$\gamma = 2\xi\sqrt{m\kappa}$$

where ξ is the effective damping ratio. Since we will eventually consider an array of beams that are all attached to the same base, it is useful to introduce the relative displacement $z(t) = x(t) - y(t)$, which represents the position of the tip of the beam relative to the base,

$$m\ddot{z} + \gamma\dot{z} + \kappa z = -m\ddot{y}, \tag{3.2}$$

where the external driving force is given in terms of the base displacement via the expression $-m\ddot{y}$.

We now consider the effect of adding magnets to the tip of the cantilever. The repelling force of two magnets whose center-to-center separation distance is d_0 is given by $F = Ad_0^p$ where A and p are determined empirically, see Section 2. The experimentally measured values for all quantities and the effective parameter values are given in Table 1. If the beams decorated with magnets are separated by a distance d_0 on the base, and we let the quantity $u_n(t)$ represent the displacement of the $n-th$ beam tip relative to its location on the base, then we arrive at the model equation of interest,

$$m\ddot{u}_n = A\left[d_0 + u_n - u_{n-1}\right]^p - A\left[d_0 + u_{n+1} - u_n\right]^p - \gamma\dot{u}_n - \kappa u_n + \beta u_n^3 + F_{\text{ext}}\cos\left(2\pi f t\right), \tag{3.3}$$

where $n = 1, \ldots, N$ and N is the number of cantilevers. The term βu_n^3 is a phenomenological term added to account for the possibility of nonlinearity in the beam [22] for the numerical considerations later in the paper. It is assumed that the base is excited harmonically with the driving frequency f_d, e.g., $y(t) = y_0\cos(2\pi f_d t)$ where y_0 is the amplitude of the excitation. Thus, the external force coefficient is given by $F_{\text{ext}} = -y_0(2\pi f_d)^2 m$. If a base excitation is introduced, the walls are assumed to be immovable so that $u_0(t) = u_{N+1}(t) = 0$. This is the situation for the experimental set-up. We also will explore numerically the possibility of boundary excitation with a non-moving base, in which case $u_0(t) = \alpha\cos(2\pi f_d t)$, $u_{N+1}(t) = 0$ and $F_{\text{ext}} = 0$.

4. Linear analysis and computation of periodic orbits and their stability

The Hamiltonian lattice corresponds to $\beta = y_0 = \gamma = 0$. To consider linearized dynamics (with $p \neq 1$) we require small amplitudes, i.e., $\frac{|u_n - u_{n+1}|}{d_0} \ll 1$, so that the magnetic coupling force can be linearized.

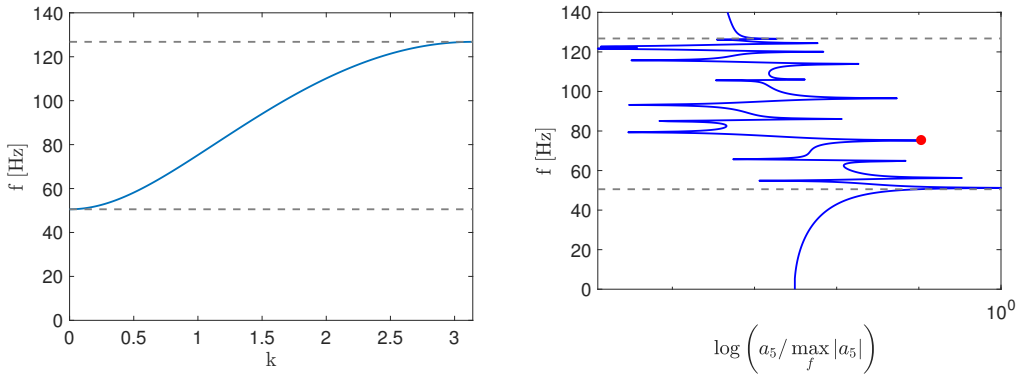

Figure 4. The dispersion relation Eq. (4.1) is shown in the left panel. The right panel shows the results of the damped-driven linear system through the amplitude response of the 5th bead a_5 ($\log(a_5/\max_{f\in[f_\ell,f_u]} a_5)$ is shown on the horizontal axis) as a function of the frequency f on the vertical axis). The frequency is shown on the vertical axis to be consistent with the left panel. The red dot corresponds to the frequency $f_d = 72.5$ Hz.

The resulting linearized Hamiltonian variant of Eq. (3.3) has plane wave solutions $u \sim \exp(i(kn + \omega t))$ where the dispersion relationship is given by

$$\omega(k)^2 = \frac{2K_2(\cos(k) - 1) + \kappa}{M} \tag{4.1}$$

where $K_2 = pAd_0^{p-1} < 0$. In the case of $N \to \infty$, i.e., an infinite lattice, $k \in [0, \pi]$, and for a lattice consisting of N (finite) nodes with zero boundary conditions $k = k_n = \frac{n\pi}{N+1}$ with $n = 1, 2, \ldots, N$. The dispersion curve in terms of frequency $f = \omega/2\pi$ is shown in Figure 4 (left). The lower and upper cutoff frequencies, $f_\ell = \omega(0)/2\pi \approx 50.6$ Hz and $f_u = \omega(\pi)/2\pi \approx 126.8$ Hz respectively, are shown as dashed lines in Figure 4.

In the damped-driven linear system, namely when $\beta = 0$, $\frac{|u_n - u_{n+1}|}{d_0} \ll 1$ and $y_0 \neq 0 \neq \gamma$ time-periodic steady-states of the form $u_n(t) = a_n \cos(2\pi f_d t + \phi_n)$ can be found explicitly, where a_n and ϕ_n are the amplitude and phase of the nth node, respectively. An example plot of a_5 for $f_d \in [0, 140]$ and $F_{\text{ext}} = 1.54 \cdot 10^{-6}$ N is shown in Figure 4 (right). The critical points correspond to the $N = 21$ linear resonant frequencies. An example linear resonance at $f \approx 75.2$ Hz is shown as a red dot in Figure 4 (right).

For the remainder of the article, we will be interested in time-periodic orbits of the nonlinear Eq. (3.3) (i.e., where the conditions $\beta = 0$ and $\frac{|u_n - u_{n+1}|}{d_0} \ll 1$ do not necessarily hold). In this case, exact analytical solutions are not available (although they can be approximated via long wavelength approximations [23]). Thus, we will turn to numerical computations. We compute time-periodic orbits of Eq. (3.3) with period $T_d = 1/f_d$ with high precision by finding roots of the map $F := \mathbf{x}(T_d) - \mathbf{x}(0)$, where $\mathbf{x}(T_d)$ is the solution of Eq. (3.3) at time T_d with initial condition $\mathbf{x}(0)$. Roots of this map (and hence time-periodic solutions of Eq. (3.3)) are found via Newton iterations. This requires the Jacobian of F, which is of the form $V(T_d) - I$, where I is the identity matrix, V is the solution to the N^2 variational equations $V' = DF \cdot V$ with initial condition $V(0) = I$, and DF is the Jacobian of the equations of motion evaluated at a given state vector of the form of $\mathbf{X} = [\mathbf{u}, \dot{\mathbf{u}}]^T$ where

$\mathbf{u} = [u_1, u_2, \ldots, u_N]^T$. Note that the solution frequency and drive frequency are both f_d by construction. An initial guess for the Newton iterations can be provided by the linear steady-state solutions $u_n(t) = a_n \cos(2\pi f_d t + \phi_n)$. To investigate the dynamical stability of the obtained states, a Floquet analysis is used to compute the multipliers associated with the solutions. The Floquet multipliers for a solution are obtained by computing the eigenvalues of the monodromy matrix (which is $V(T_b)$ upon convergence of the Newton scheme). If a solution has all Floquet multipliers on the unit circle, the solution is called (spectrally) stable. An instability that is result of a multiplier on the (positive) real line is called a real (exponential in nature) instability. However, there can also be oscillatory instabilities, which correspond to complex-conjugate pairs of Floquet multipliers lying outside the unit circle (in the complex plane). In the bifurcation diagrams that are to follow in this paper, solid blue segments will correspond to stable parametric regions while the dashed red segments correspond to real unstable regions and green dashed-dotted segments correspond to oscillatorily unstable regions. The bifurcation diagrams are obtained using a pseudo-arclength continuation algorithm.

5. Model validation

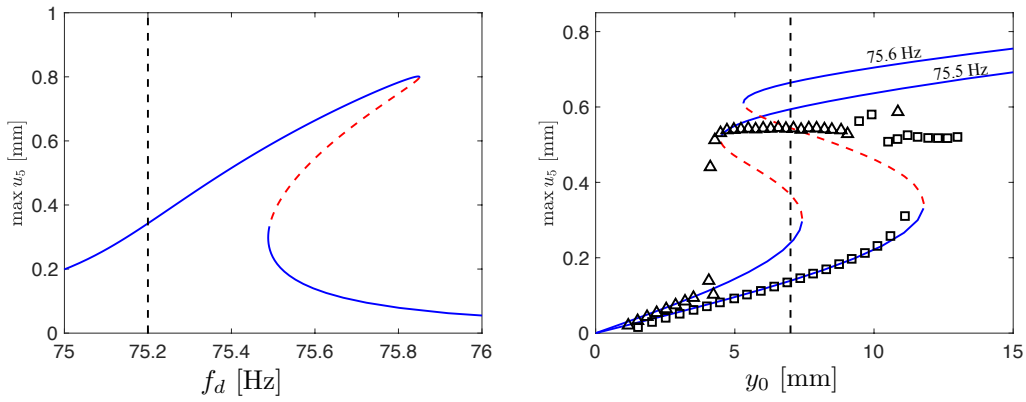

Figure 5. The left panel corresponds to continuation results over the driving frequency f_d. In particular, the maximum (over one period) position of the fifth bead, i.e., u_5 is monitored as a function of f_d. The vertical black dashed line corresponds to a value of the frequency of 75.2 Hz. The right panel shows the maximum (again over one period) of u_5 as a function of the excitation amplitude of the base, i.e., y_0 for two nearly close driving frequencies of $f_d = 75.6$ Hz and $f_d = 75.5$ Hz. Note that black markers correspond to experimental results. In the experiments and simulations shown here, there are $N = 21$ nodes.

We now present experimental data that demonstrate that Eq. (3.3) is a reasonable model for the cantilever array decorated with magnets.

In the experiment, we perform amplitude sweeps at a fixed frequency (in particular at $f_d = 75.2$ Hz, which is close to a resonant frequency, see the red dot in Figure 4). In particular, we let the system settle to steady-state for a fixed frequency (and the steady-state amplitude is recorded) and then the drive amplitude is changed slightly and we let the system once again reach steady-state, etc. The

experimental results are shown in Figure 5 (right), where the upward sweep is shown as square markers and the downward sweep is shown as triangles. The hysteretic behavior identified in the experiments reveals that the system is bistable for various values of the base excitation amplitude (see e.g., the dashed line at 7μm of Figure 5 (right)). To validate our model, we performed a similar procedure theoretically. In particular, we carried out a pseudo-arclength continuation of time-periodic solutions of Eq. (3.3) with respect to the amplitude y_0 and the drive frequency fixed to $f_d = 75.2$ Hz (other parameter values are given in Table 1). However, no region of bistability is found, suggesting a slight mistuning of our system parameter values. To investigate this further, a pseudo-arclength continuation with respect to the drive frequency f_d was performed for Eq. (3.3) with the base excitation amplitude fixed to $y_0 = 7\mu$m, see Figure 5 (left). Note the pseudo-arclength continuation allows us to follow theoretically not only the stable branches (solid blue lines) of the bistable response, but also the unstable ones in between (red dashed lines). It is clear from Figure 5 (left) that the region of bistability is for drive frequencies larger than $f_d = 75.2$ Hz. For this reason, we revisited the drive amplitude continuation, but for frequencies slightly larger than 75.2 Hz. In particular, we conducted a pseudo-arclength continuation of time-periodic solutions of Eq. (3.3) with respect to the amplitude y_0 and the drive frequency fixed to $f_d = 75.5$ Hz and $f_d = 75.6$ Hz (see the curves of Figure 5 (right)). Notice that the $f_d = 75.6$ Hz continuation matches the forward sweep and the $f_d = 75.5$ Hz continuation matches the backward sweep. Ideally, both the forward and backward sweeps in the experiments should match a continuation for a single frequency. Thus, while the qualitative behavior is captured overall, in our model it is only possible to (quantitatively) fit one direction.

6. Numerical exploration of the system

Since we demonstrated in the previous section that Eq. (3.3) is a good model for the array of cantilevers decorated with magnets, we will proceed to carry out a more detailed numerical exploration of the system. In the subsequent section, comparisons of boundary and base excitation will be made. In Section 6.2 breather solutions of a lattice with a defect are explored.

6.1. Comparing boundary and base excitation

To draw comparisons to systems that are typically driven on the boundary, such as the granular chain, we will now conduct numerical continuations with $F_{\text{ext}} = u_{N+1} = 0$ and $u_0 = \alpha\cos(2\pi f_d t)$. The parameter values for the subsequent comparison of boundary and base excitation are shown in Table 2. We chose different parameter values than in Section 5 to demonstrate how the solutions of the base excitation problem can vary with a different parameter set.

A linear analysis of the resonant peaks will reveal that the most dominant mode in the base excitation problem corresponds to in-phase motion (associated with the lowest frequency response peak), as expected. The modal contributions in the boundary excitation problem are more distributed. This is also reflected in the resonant peaks of the nonlinear system which were found by performing a pseudo-arclength continuation in the drive frequency f_d, see Figure 6. For the base excitation, the amplitude is fixed to $F_{\text{ext}} = 0.028$ N (recall that $F_{\text{ext}} = -y_0(2\pi f_d)^2 m$). To make a comparison of the same magnitude in the boundary excitation problem, the amplitude is fixed to $\alpha = 46.368$ μm, which corresponds to an approximate maximum force contribution of $pA(d_0)^{p-1}\alpha \approx 0.022$ N. In addition to how the magnitude of the resonant peaks differs between the two excitation problems, the boundary

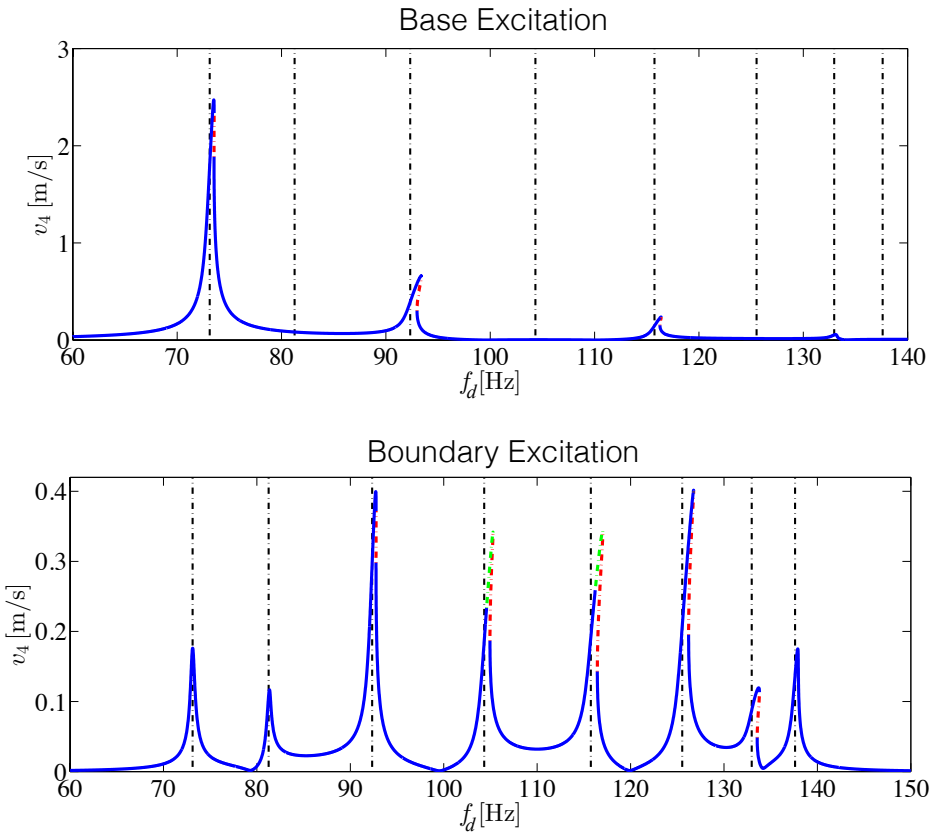

Figure 6. Top: Nonlinear resonances for the base excitation problem. The maximum velocity of node 4 (over one period $T_d = 1/f_d$), i.e., $v_4 = \max_{t\in[0,T_d]} \dot{u}_4(t)$, is shown as a function of the driving frequency f_d for the fixed driving amplitude of $F_{\text{ext}} = 0.028$ N. The blue solid lines correspond to stable regions, where as the red dashed lines indicate a real instability. The vertical dashed-dotted black lines correspond to the linear resonances. The lowest frequency peak corresponds to in-phase motion. Bottom: Same as the top panel, but for the boundary excitation problem. v_4 is shown as a function of the driving frequency f_d for the fixed driving amplitude of $\alpha = 46.368\mu$m. The green dash-dotted line corresponds to regions with an oscillatory instability. In the simulations shown here, there are $N = 8$ nodes.

Table 2. Parameter values used for comparing the base and boundary excitation problem.

Parameter	Value
p	-3.834
N	8
A	$1.05534668 \times 10^{-8}$ N/m^p
γ	1.0105×10^{-2} Ns/m
κ	696.1 N/m
m	3.59 g
d	8.13 mm
β	0

excitation problem differs in its stability properties. In the base excitation problem, no regions of oscillatory instability were identified (as seen in Figure 6 (top), but also in other similar computations we have made). This is in contrast to the boundary excitation problem, where oscillatory instabilities appear generically (as seen in Figure 6 (bottom), but also in other similar computations we have made). Another important difference is that the instability regions invade (some of) the higher amplitude branches of the resonant peaks in the boundary excitation problem (in Figure 6 (bottom) oscillatory instabilities are present for higher frequency peaks). Thus, while the distribution of the modes in the boundary excitation problem is potentially more appealing from a potential application perspective (for example in the energy harvesting context [22]), this problem is more unstable than the base excitation problem. This latter aspect is even more apparent when inspecting the bifurcation diagram for the amplitude continuation (with f_d fixed), see Figure 7. In the base excitation problem the higher amplitude branch is stable, whereas in the boundary excitation problem the higher amplitude branch becomes unstable (via an oscillatory instability) at some critical amplitude (in the case of the right panel of Figure 7 at $\alpha \approx 60$) and does not regain stability. Example solution profiles (corresponding to the letter labels of Figure 7) and their Floquet multiplier spectra for the base and boundary excitation problems are given in Figures 8 and 9, respectively.

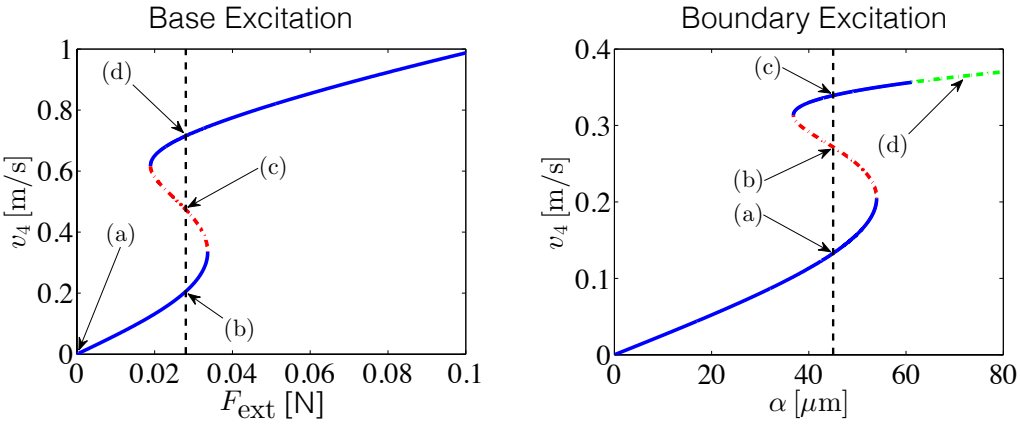

Figure 7. The left panel presents the maximal velocity of the 4th bead v_4 (over one period of motion) as a function of the amplitude of the base drive F_{ext} for $f_d = 93.3$ Hz. Note that the vertical dashed-dotted black line corresponds to the value of $F_{\text{ext}} = 0.028$ N, see the top panel of Figure 6. The right panel presents the velocity of the 4th bead v_4 (over one period of motion) as a function of the amplitude of the boundary drive α for $f_d = 126.3$ Hz. Note that the vertical dashed-dotted black line corresponds to the value of $\alpha = 46.368\,\mu$m, see the bottom panel of Figure 6. The letter labels in both panels correspond to the solution profiles shown in Figures 8 and 9. In the simulations shown here, there are $N = 8$ nodes.

6.2. Breathers in a defect lattice

We will now turn our attention to breather solutions of this system, namely ones that are time-periodic and localized in space. To introduce a localized mode into the system, a light mass defect is added to the center of the chain. In particular, the effective mass of all the particles is the same as

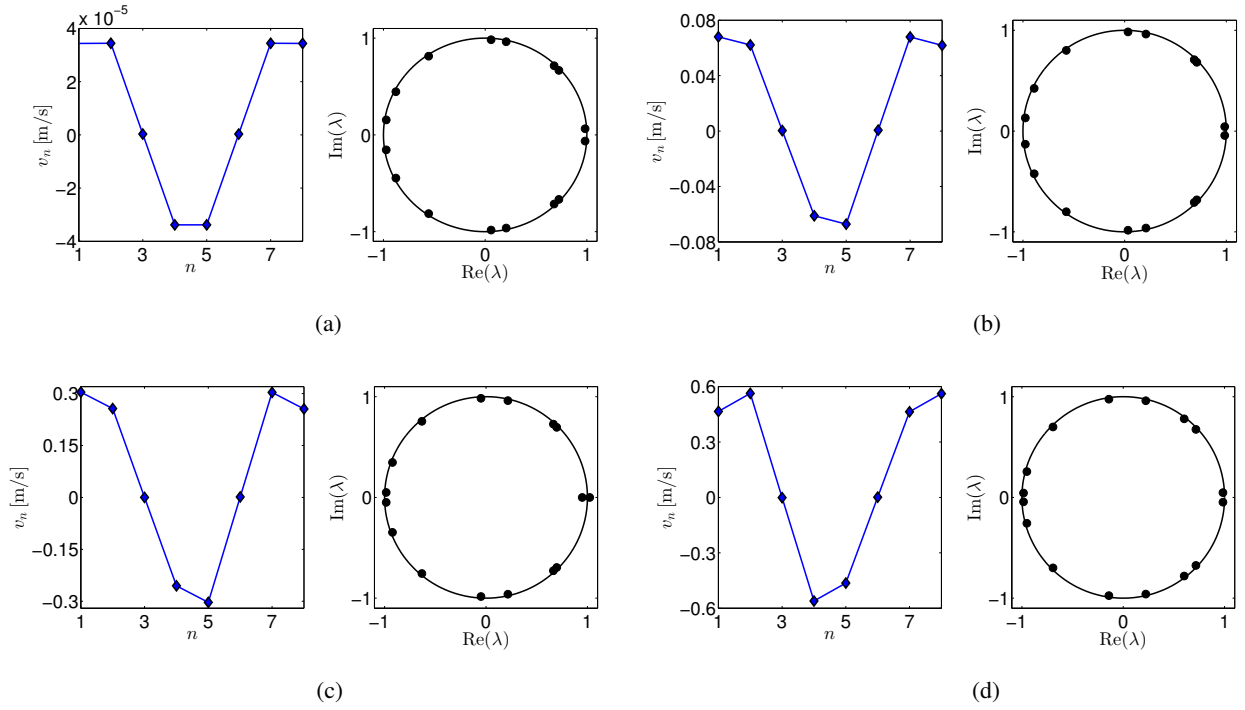

Figure 8. (Color online) Velocity profiles and corresponding Floquet multipliers of time-periodic solutions obtained at a driving frequency of $f_d = 93.3\,\text{Hz}$ and for various values of the excitation amplitude of (a) $F_{\text{ext}} = 2 \times 10^{-5}\,\text{m}$ and (b)–(d) $F_{\text{ext}} = 0.028\,\text{m}$. Note that the results presented herein are associated with the left panel of Figure 7. In the simulations shown here, there are $N = 8$ nodes.

before (namely the effective mass is 3.59 g) however the center particle has an effective mass of 1.795 g. Since the breather solutions we are seeking will be a result of this mass defect, the breathers can also be thought of as nonlinear localized modes [24]. By the term "breathers", we will refer to exponentially localized in space, periodic in time solutions more generally, without necessitating that the underlying lattice system be homogeneous in space. While breathers that are the result of modulation instability (MI) of plane waves from the bottom of the spectral band are possible in the Hamiltonian system (also called intrinsic localized modes), our system is highly damped, and thus obtaining breathers through MI was not possible. Other than this mass defect, and the lattice size which we take to be $N = 21$ in this section, all parameters are the same as those in Table 2 and we only consider base excitation. The nonlinear resonant peaks of this system are shown in Figure 10. Similar to the top panel of Figure 6, the peak corresponding to the in-phase mode is fairly dominant. However, there is now a resonant peak in the gap, which corresponds to the localized defect mode. A zoom of the defect mode resonant peak is shown in the left panel of Figure 11. With the drive frequency fixed to $f_d = 174\,\text{Hz}$ (see the dashed line in the left panel of Figure 11) an amplitude continuation is also performed, see the right panel of Figure 11. Note, in [25] a similar situation was explored in the context of a granular chain with a single light mass defect that is driven on one boundary. There the higher amplitude solutions in the drive amplitude continuation are unstable (similar to the right panel of Figure 7). At the drive amplitudes where the breathers are oscillatorily unstable, quasi-periodic solutions are approached. In

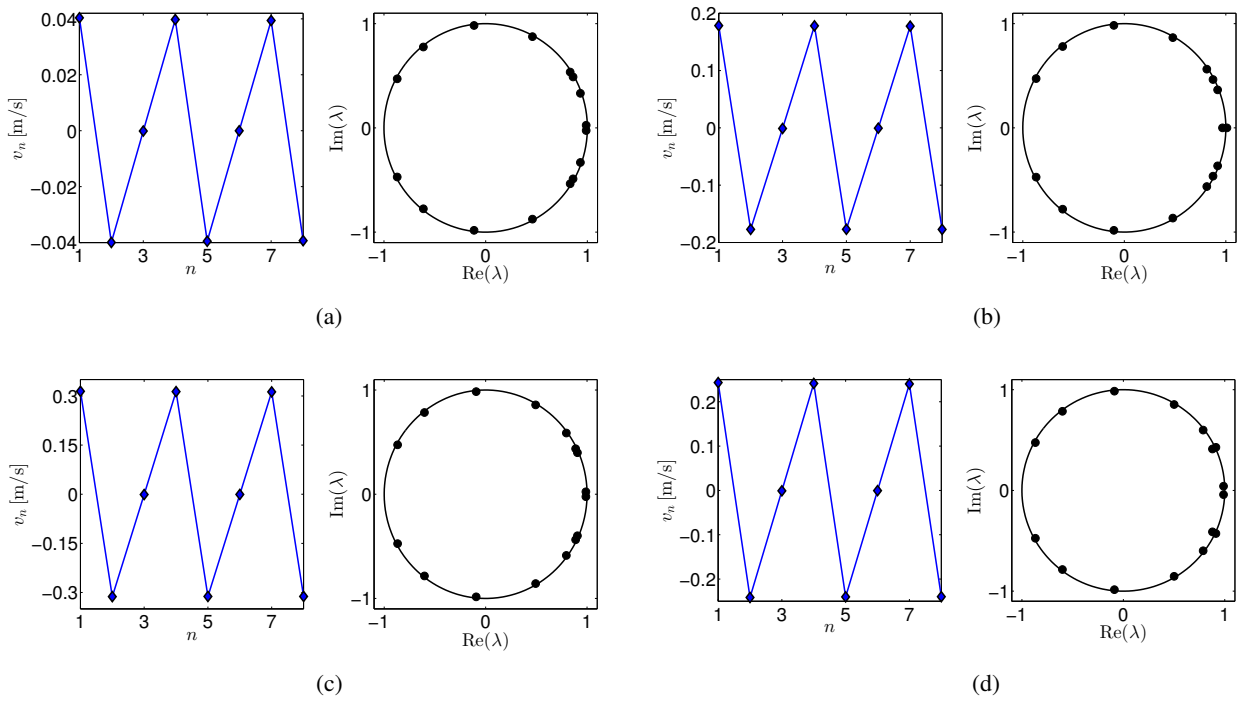

Figure 9. (Color online) Same as Figure 8 but for the case with left boundary excitation. Velocity profiles and corresponding Floquet multipliers of time-periodic solutions obtained at a driving frequency of $f_d = 126.3$ Hz and for various values of the excitation amplitude of (a)–(c) $\alpha = 45\,\mu$m and (d) $\alpha = 72\,\mu$m. The solution in panel (d) features an oscillatory instability. Note that the results presented herein are associated with the right panel of Figure 7. In the simulations shown here, there are $N = 8$ nodes.

our base excited system, the high amplitude breathers are stable, and thus, the system is not driven to quasi-periodicity. Example breather profiles (corresponding to the letter labels of the right panel of Figure 11) and their Floquet multiplier spectra are given in Figure 12. Note the asymmetry of the spatial profiles of the solutions shown in Figure 12. This is a consequence of the asymmetric nature of the interaction potential. This can be seen through a Taylor expansion of the magnetic force, leading to both quadratic and cubic force terms. In nonlinear lattices with cubic terms only, the potential is symmetric, and hence the profiles are also symmetric [26].

The final numerical experiment considers non-zero values of the onsite nonlinear force coefficient β. Bistability of the defect breather is possible for zero, negative, and positive values of β, see Figure 13. Example breather profiles (corresponding to the letter labels of Figure 13) and their Floquet multiplier spectra are given in Figure 14. Note the bifurcation values (i.e., the turning points in Figure 13) occur for very large values of β. This is due to the fact that the beam deflections are somewhat small, and hence a large value of β is required for the nonlinear term to have an effect on the system. A more physically realistic scenario where the beam nonlinearity would be observed is in the case of large deflections. This would require the equilibrium distance d_0 to be larger (in order to allow "room" for

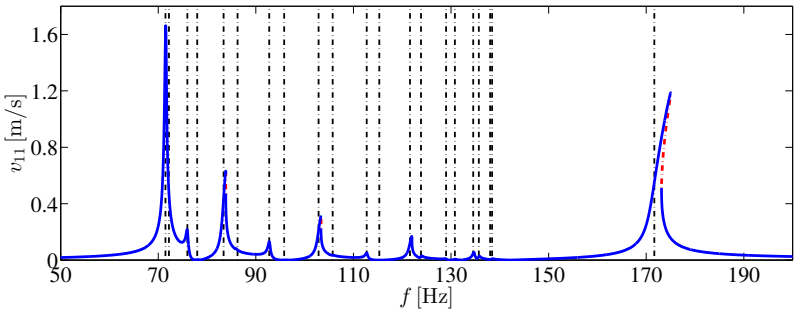

Figure 10. Nonlinear resonant peaks of the base excitation problem with a single light mass defect at node $n = 11$. The drive amplitude is fixed to $F_{\text{ext}} = 0.023184$ N. The maximum velocity of bead 11 is shown as a function of the driving frequency f_d. The black vertical dashed lines correspond to the linear resonances. Notice the somewhat dominant resonant peak in the stop-band, which corresponds to the (defect induced) breather. In the simulations shown here, there are $N = 21$ nodes.

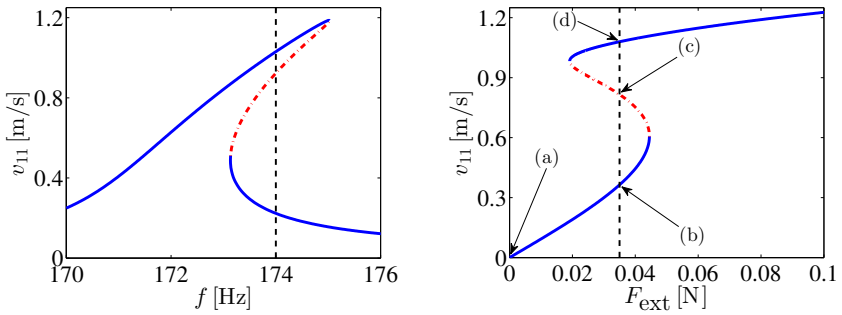

Figure 11. The left panel is a zoom in of the defect resonant peak shown in Figure 10 where the vertical dashed-dotted black line corresponds to a value of the driving frequency of $f_d = 174$ Hz. The right panel presents the velocity of the 11th bead v_{11} (over one period of motion) as a function of the amplitude of the external drive F_{ext} for $f_d = 174$ Hz. Note that the vertical dashed-dotted black line corresponds to a value of F_{ext} of 0.035 m. In the simulations shown here, there are $N = 21$ nodes.

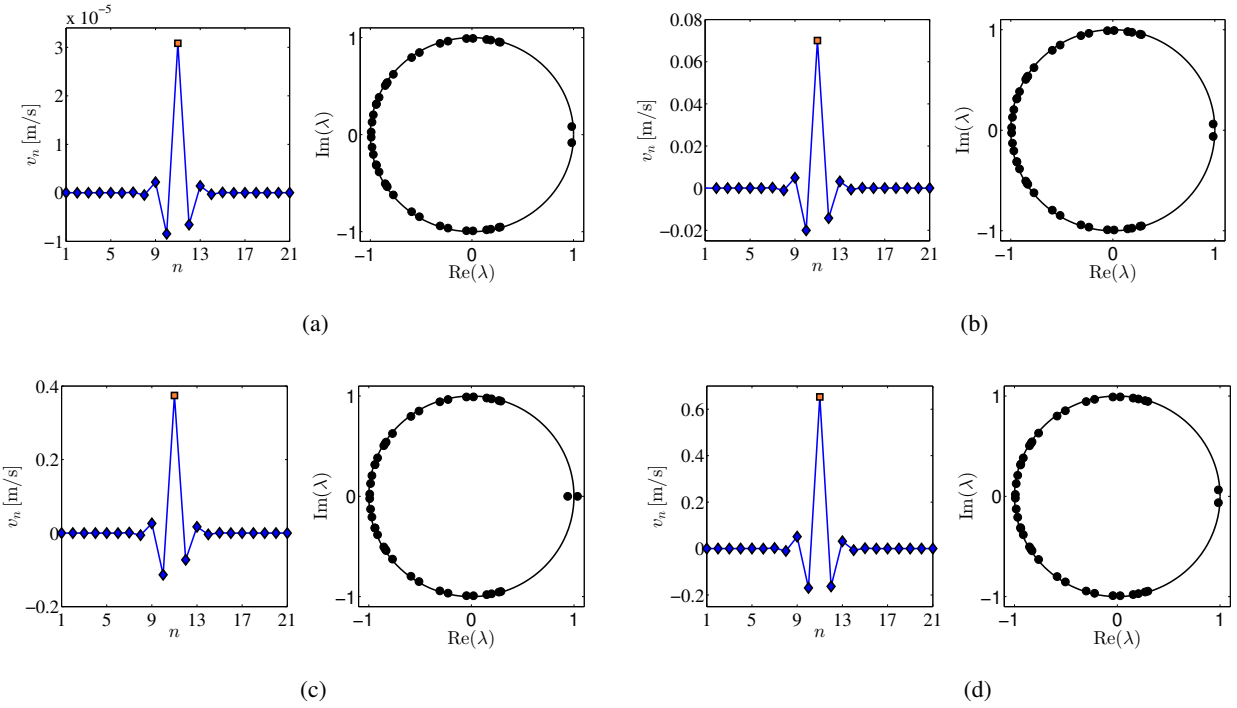

Figure 12. (Color online) Velocity profiles and corresponding Floquet multipliers of breathers in the base excitation problem with a single light mass defect. The driving frequency is fixed to $f_d = 174\,\text{Hz}$ and various values of the excitation amplitude are shown: (a) $F_{\text{ext}} = 2 \times 10^{-5}\,\text{m}$ and (b)–(d) $F_{\text{ext}} = 0.035\,\text{m}$. Note that the results presented herein are associated with the right panel of Figure 11. In the simulations shown here, there are $N = 21$ nodes.

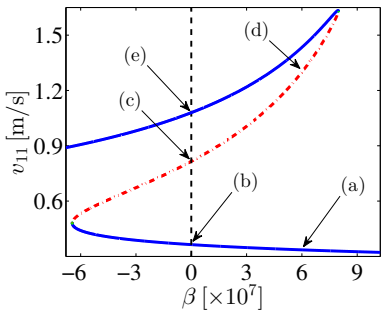

Figure 13. The bifurcation diagram corresponding to the maximum velocity of bead 11 (over one period $T = 1/f$) as a function of the parameter β with $f_d = 174\,\text{Hz}$ and $F_{\text{ext}} = 0.035\,\text{m}$. In the simulations shown here, there are $N = 21$ nodes.

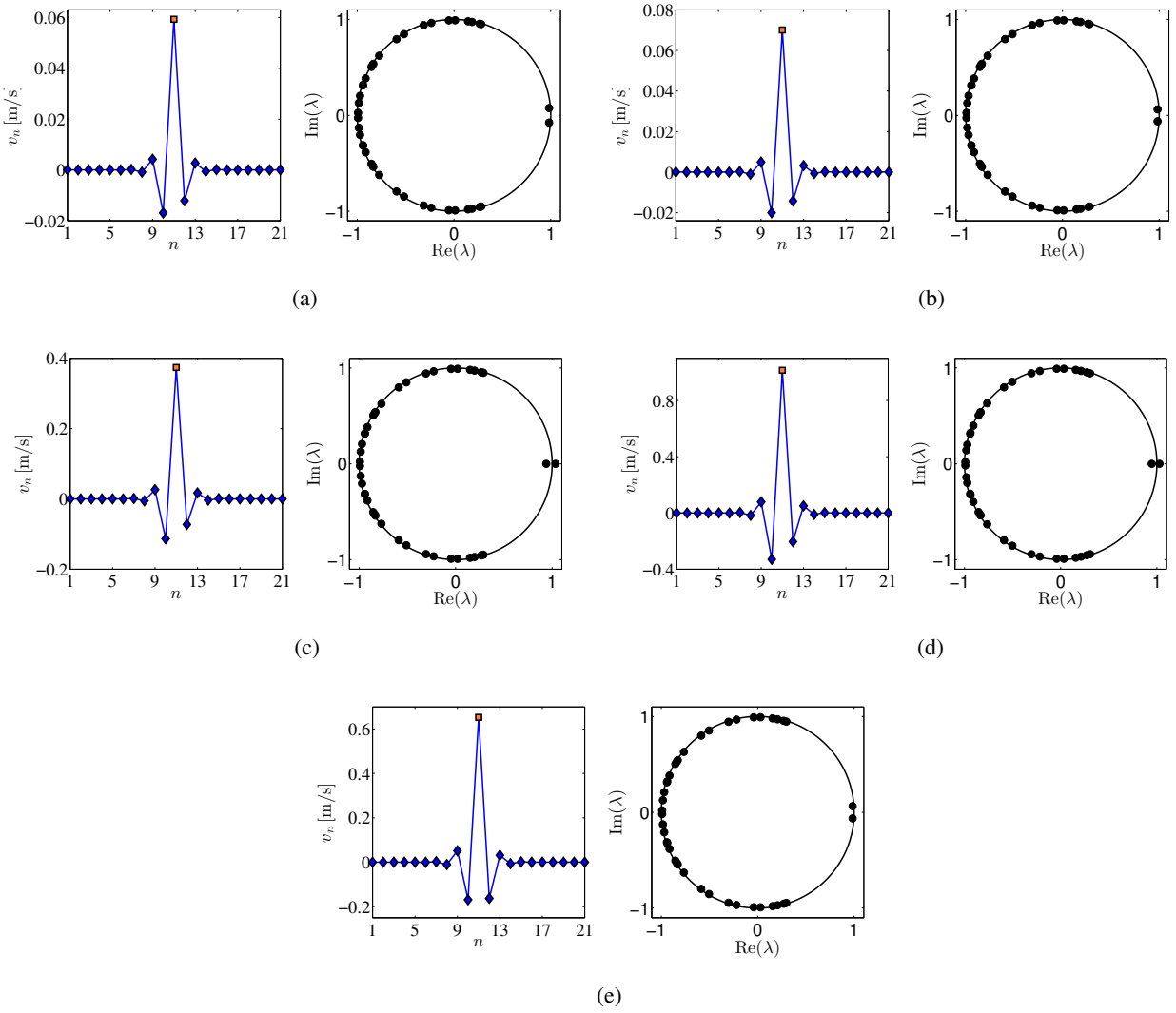

Figure 14. (Color online) Velocity profiles and corresponding Floquet multipliers of breathers obtained at a driving amplitude and frequency of $F_{\text{ext}} = 0.035$ m and $f_d = 174$ Hz, respectively and for various values of β: (a) and (d) $\beta = 6 \times 10^7$ and (b)–(e) $\beta = 0$. Note that the results presented herein are associated with Figure 13. In the simulations shown here, there are $N = 21$ nodes.

the beams to have large deflections). If we rescale the problem via

$$t \to \eta t, \quad u_n \to d_0 u_n, \qquad \eta = \sqrt{\frac{A d_0^{p-1}}{m}} \tag{6.1}$$

then $A/m = d_0 = 1$ and $\beta \to \beta \frac{d_0^2}{\xi^2}$. Here we see that if we increase the dimensional d_0 by, e.g., a factor 15, then according to the above, the coefficient for the onsite cubic nonlinearity is 8 orders of magnitude larger (note the amplitude of the external force increases about 4 orders of magnitude). Thus, while the bifurcation values in Figure 13 seem very large, they have a reasonable physical interpretation, if e.g., considering large deflections. Although such large deflections may be hard to realize with the cantilevers considered in our experiment, other similar systems, such as the one the studied in [27], would allow such large deflections.

7. Conclusion

We have introduced a system consisting of an array of cantilevers that are coupled via magnetic links and demonstrated that the damped-driven mixed FPTU-KG model provides a reasonably good description of the dynamics observed in the experiments. This article focused on the topic of time-periodic solutions (and their breather variants), both for the case of base and boundary excitation, and also in the presence of a light mass defect. The bistable response of the system and the possibility of hysteresis were featured both in our numerical and in our experimental results, in qualitative agreement between the two.

Nevertheless, there are many other avenues for future research that this system inspires. One includes revisiting the Hamiltonian variant of the problem to study how the stability of Hamiltonian breathers is affected as the strength of the nonlinear parameter β varies and contrast this to the case where the intersite nonlinearity is a polynomial (as in [20]) as opposed to a power-law, as in our paper. Higher dimensional analogs of this system, in e.g., hexagonal or square configurations, would also be worth exploring. Finally, the robustness of this system for the purposes of applications, such as energy harvesting, would be another important research direction.

Acknowledgments

This material is based upon work supported by the National Science Foundation under Grant No. DMS-1615037 (CC) and DMS-1809074 (PGK). CC would like to thank Carina Spiro and Jacob Hart of Bowdoin College and Chenzhang Zhou of the École Polytechnique for technical assistance. EGC would like to thank the Department of Mathematics at Bowdoin College for the kind hospitality where the initial stages of this work were carried out. PGK gratefully acknowledges support from the US-AFOSR via FA9550-17-1-0114.

Conflict of interest

The authors declare no conflict of interest.

References

1. Gallavotti G (2008) *The Fermi–Pasta–Ulam Problem: A Status Report*. Heidelberg: Springer-Verlag.
2. Kevrekidis PG (2011) Non-linear waves in lattices: Past, present, future. *IMA J Appl Math* 76: 389–423.
3. Lederer F, Stegeman GI, Christodoulides DN, et al. (2008) Discrete solitons in optics. *Phys Rep* 463: 1–126.
4. Binder P, Abraimov D, Ustinov AV, et al. (2000) Observation of breathers in Josephson ladders. *Phys Rev Lett* 84: 745–748.
5. Trías E, Mazo JJ, Orlando TP (2000) Discrete breathers in nonlinear lattices: Experimental detection in a Josephson array. *Phys Rev Lett* 84: 741–744.
6. English LQ, Sato M, Sievers AJ (2003) Modulational instability of nonlinear spin waves in easy-axis antiferromagnetic chains. II. Influence of sample shape on intrinsic localized modes and dynamic spin defects. *Phys Rev B* 67: 024403.
7. Schwarz UT, English LQ, Sievers AJ (1999) Experimental generation and observation of intrinsic localized spin wave modes in an antiferromagnet. *Phys Rev Lett* 83: 223–226.
8. Swanson BI, Brozik JA, Love SP, et al. (1999) Observation of intrinsically localized modes in a discrete low-dimensional material. *Phys Rev Lett* 82: 3288–3291.
9. Peyrard M (2004) Nonlinear dynamics and statistical physics of DNA. *Nonlinearity* 17: R1–R40.
10. Morsch O, Oberthaler M (2006) Dynamics of Bose-Einstein condensates in optical lattices. *Rev Mod Phys* 78: 179–215.
11. Nesterenko VF (2001) *Dynamics of Heterogeneous Materials*. New York: Springer-Verlag, USA.
12. Chong C, Kevrekidis P (2018) *Coherent Structures in Granular Crystals: From Experiment and Modelling to Computation and Mathematical Analysis*. Heidelberg: Springer.
13. Starosvetsky Y, Jayaprakash KR, Hasan MA, et al. (2017) *Dynamics and Acoustics of Ordered Granular Media*. Singapore: World Scientific.
14. Rosas A, Lindenberg K (2018) Pulse propagation in granular chains. *Phys Rep* 735: 1–37.
15. Chong C, Porter MA, Kevrekidis PG, et al. (2017) Nonlinear coherent structures in granular crystals. *J Phys Condens Matter* 29: 413002.
16. Sen S, Hong J, Bang J, et al. (2008) Solitary waves in the granular chain. *Phys Rep* 462: 21–66.
17. Bonanomi L, Theocharis G, Daraio C (2015) Wave propagation in granular chains with local resonances. *Phys Rev E* 91: 033208.
18. Lydon J, Serra-Garcia M, Daraio C (2014) Local to extended transitions of resonant defect modes. *Phys Rev Lett* 113: 185503.
19. James G (2011) Nonlinear waves in Newton's cradle and the discrete p-Schrödinger equation. *Math Models Methods Appl Sci* 21: 2335–2377.
20. Kimura M, Hikihara T (2008) Stability change of intrinsic localized mode in finite nonlinear coupled oscillators. *Phys Lett A* 372: 4592–4595.

21. Sato M, Hubbard BE, Sievers AJ (2006) *Colloquium*: Nonlinear energy localization and its manipulation in micromechanical oscillator arrays. *Rev Mod Phys* 78: 137–157.

22. Erturk A, Inman DJ (2011) *Piezoelectric Energy Harvesting*. Hoboken: Wiley & Sons.

23. Giannoulis J, Mielke A (2004) The nonlinear Schrödinger equation as a macroscopic limit for an oscillator chain with cubic nonlinearities. *Nonlinearity* 17: 551–565.

24. Theocharis G, Kavousanakis M, Kevrekidis PG, et al. (2009) Localized breathing modes in granular crystals with defects. *Phys Rev E* 80: 066601.

25. Boechler N, Theocharis G, Daraio C (2011) Bifurcation based acoustic switching and rectification. *Nat Mater* 10: 665–668.

26. Huang G, Shi ZP, Xu Z (1993) Asymmetric intrinsic localized modes in a homogeneous lattice with cubic and quartic anharmonicity. *Phys Rev B* 47: 14561–14564.

27. Nadkarni N, Arrieta AF, Chong C, et al. (2016) Unidirectional transition waves in bistable lattices. *Phys Rev Lett* 116: 244501.

AIMS Press